



Article

Adsorption and Release of Sulfamethizole from Mesoporous Silica Nanoparticles Functionalised with Triethylenetetramine

Cristina Carucci ^{1,2} , Nicola Scalas ¹, Andrea Porcheddu ¹ , Marco Piludu ^{2,3}, Maura Monduzzi ^{1,2} and Andrea Salis ^{1,2,*}

¹ Dipartimento di Scienze Chimiche e Geologiche, Università di Cagliari, Cittadella Universitaria, SS 554 Bivio Sestu, 09042 Monserrato, CA, Italy; cristina.carucci@unica.it (C.C.); nicola.scalas@tiscali.it (N.S.); porcheddu@unica.it (A.P.); monduzzi@unica.it (M.M.)

² Consorzio Interuniversitario per lo Sviluppo dei Sistemi a Grande Interfase (CSGI), via Della Lastruccia 3, 50019 Sesto Fiorentino, FI, Italy; mpiludu@unica.it

³ Dipartimento di Scienze Biomediche, Università di Cagliari, Cittadella Universitaria, SS 554 Bivio Sestu, 09042 Monserrato, CA, Italy

* Correspondence: asalis@unica.it; Tel.: +39-070-675-4362

Abstract: Mesoporous silica nanoparticles (MSN) were synthesised and functionalised with triethylenetetramine (MSN-TETA). The samples were fully characterised (transmission electron microscopy, small angle X-ray scattering, Fourier transform infrared spectroscopy, thermogravimetric analysis, zeta potential and nitrogen adsorption/desorption isotherms) and used as carriers for the adsorption of the antimicrobial drug sulphamethizole (SMZ). SMZ loading, quantified by UV-Vis spectroscopy, was higher on MSN-TETA (345.8 mg g⁻¹) compared with bare MSN (215.4 mg g⁻¹) even in the presence of a lower surface area (671 vs. 942 m² g⁻¹). The kinetics of SMZ adsorption on MSN and MSN-TETA followed a pseudo-second-order model. The adsorption isotherm is described better by a Langmuir model rather than a Temkin or Freundlich model. Release kinetics showed a burst release of SMZ from bare MSN samples ($k_1 = 136 \text{ h}^{-1}$) in contrast to a slower release found with MSN-TETA ($k_1 = 3.04 \text{ h}^{-1}$), suggesting attractive intermolecular interactions slow down SMZ release from MSN-TETA. In summary, the MSN surface area did not influence SMZ adsorption and release. On the contrary, the design of an effective drug delivery system must consider the intermolecular interactions between the adsorbent and the adsorbate.

Keywords: MSN; antimicrobial drug; adsorption; kinetics; isotherms; release



Citation: Carucci, C.; Scalas, N.; Porcheddu, A.; Piludu, M.; Monduzzi, M.; Salis, A. Adsorption and Release of Sulfamethizole from Mesoporous Silica Nanoparticles Functionalised with Triethylenetetramine. *Int. J. Mol. Sci.* **2021**, *22*, 7665. <https://doi.org/10.3390/ijms22147665>

Academic Editor: Bice Conti

Received: 12 May 2021

Accepted: 14 July 2021

Published: 17 July 2021

Publisher's Note: MDPI stays neutral with regard to jurisdictional claims in published maps and institutional affiliations.



Copyright: © 2021 by the authors. Licensee MDPI, Basel, Switzerland. This article is an open access article distributed under the terms and conditions of the Creative Commons Attribution (CC BY) license (<https://creativecommons.org/licenses/by/4.0/>).

1. Introduction

The goal of an efficient drug delivery system (DDS) is to directly transport the correct amount of therapeutic molecules to the target with a tailored and controlled release [1]. Among nanocarriers for in situ drug delivery, mesoporous silica nanoparticles (MSNs) are likely one of the most promising [2,3]. MSNs have a regular highly reproducible, ordered, mesoporous structure constituted by cylindrical pores (pore size 2–5 nm), with a high surface area (~700–1000 m² g⁻¹) that provides high drug loadings [4]. MSN surface functionalisation plays more than one important role, increasing their biocompatibility [5], inserting targeting molecules [6] as well as hosting stimuli-responsive moieties [7,8]. Among various types of MSN, MCM-41 (Mobile Composition of Matter No. 41) has been widely studied in biomedicine [9], thanks to their ordered parallel pore channels that facilitate drug diffusion [10–13]. For all these reasons, many studies have explored the use of functionalised MSNs (with MCM-41 matrix) as drug delivery systems for a wide range of applications such as anticancer [14], antiviral [15] antituberculosis [16], anti-inflammatory [17], antihypertensive [18], and antibacterial treatments [19–26]. For example, Lu et al. reported high tumour suppression effect in vivo of camptotecin loaded on MSN for cancer cells target [27]. To develop an antiviral DDS, Lee and co-workers modified MSNs with glycosaminoglycan

to inhibit the viral entry of herpes simplex virus [28]. In vitro release of Rifampin, an anti-tuberculosis drug, was tested from bare MSN achieving up to 95% drug release in 24 h [16]. In another work, Gounani et al. loaded polymyxin B on MSNs obtaining a high antibacterial efficiency and an improved biocompatibility of the DDS [29].

Nowadays, antibiotic resistance is one of the biggest health threats [30]. Infections caused by bacteria resistant to common antibiotics have become a global healthcare problem in the 21st century. By 2050, the development of antibiotic-resistant bacteria will cause severe infections difficult to diagnose and treat [31,32]. Common health treatments are at risk due to superbugs (multi-drug resistant bacteria) that persist in hospitals (i.e., methicillin-resistant *Staphylococcus aureus*) [33].

Among other antimicrobial drugs of high and very high importance such as glycopeptides, lipopeptides, penicillins, quinolones [34], sulphonamides have been studied as bacteriostatic drugs, particularly against the hard-to-treat resistant bacteria resulting in nosocomial infections [35]. Sulphonamides inhibit the enzymatic synthesis of folic acid by competing with the natural substrate p-aminobenzoic acid of dihydropteroate synthase, thus reducing the effective enzyme activity [36]. Folic acid is an essential nutrient necessary for protein and nucleic acid synthesis (DNA and RNA) in bacteria cells. As a result of folic acid biosynthesis inhibition, bacterial cells stop growing, preventing their reproduction and infectivity [37,38]. Sulphonamide drugs are also used as topical ointment for burn wounds [39]. Among them sulphamethizole (SMZ) is a drug used in the treatment of urinary tract infections [40].

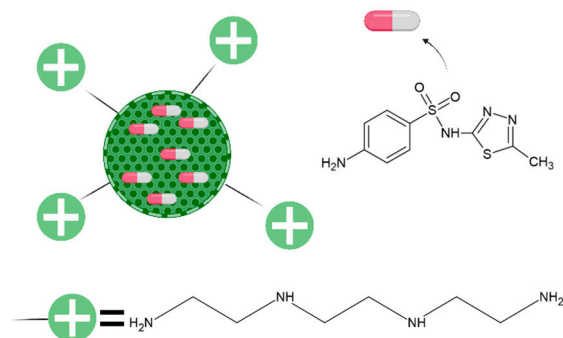
Several research papers investigated the drug delivery of sulphonamides. Ghedini et al. studied a DDS for the controlled release of silver sulphadiazine for topical administration from hybrid gels using chitosan and silica as precursors [41]. Recently, Rosas et al. studied the release of the same compound from MIL-53(Al) MOFs reaching up to 80% release in physiological conditions [42]. Suman et al. reported the impregnation of silver sulphadiazine on SBA-15 mesoporous silica reaching a 95% release in simulated body fluid after 48 h [43].

According to Vallet-Regí and co-workers, tailored functionalisation of silica nanoparticles is fundamental in developing the third generation DDS [21,44–46]. Owing to the strong presence of peptidoglycan and phosphate groups, most bacterial cell walls are negatively charged. Hence, positively charged nanoparticles may interact with bacteria cell walls through electrostatic forces. Casey et al. analysed the bacterial viability with three different types of functionalised MSNs, amine (positive), carboxylic (negative) and aromatic (neutral) finding that the positively charged functionalisation resulted in a reduction of *Staphylococcus aureus* biofilms [47]. Similarly, Zaharudin et al. analysed the loading and release of quercetin and gemcitabine from functionalised MSN-NH₂, MSN-SH and MSN-COOH [48]. Through the same antibacterial mechanism, Niu et al. coated silver core MSN with a cationic polymer QPEI (quaternary ammonium polyethyleneimine). Owing to the high positive charge of the so-constructed Ag@MSN-QPEI, the DDS showed antibacterial effect against Gram negative *Pseudomonas syringae* [49]. Dendrimers of third generation (G3), composed of high concentration of positively charged amino groups, were also used as external MSN functionalisation resulting in exceptional disruption of *E.Coli* biofilm [19]. Mas et al. decorated MSN with n-[(3-trimethoxysilyl)propyl]ethylenediamine triacetic acid trisodium salt and with the cationic polymer ϵ -poly-L-lysine. The obtained positively charged DDS was loaded with rhodamine or vancomycin resulting in an antimicrobial nanodevice with high toxicity towards Gram negative *E.Coli* [50]. All those studies point out the importance of positively charged groups grafted on the external surface of MSNs.

The triethylenetetramine (TETA) molecule possess four amino groups that are easily protonated at physiological pH [51,52]. Rotello et al. showed that gold nanoparticles functionalised with TETA become positively charged and can efficiently load siRNA, serving as an antiviral DDS [53]. Unlike long-chain functionalisation moieties, which might clog MSN mesopores and thus negatively affect the drug adsorption and release,

short-chained TETA might be a promising candidate as a positively charged functionalising agent for new DDS.

This work aims to prepare TETA functionalised-MSNs as carriers for the delivery of antimicrobial drugs (Scheme 1) [54]. To this purpose, a model drug, SMZ, was adsorbed on MSN-TETA and for comparison on bare MSNs. The samples were characterised through TEM, SAXS, FTIR, TGA, ELS and N₂ adsorption/desorption isotherms. The kinetics and thermodynamics of SMZ adsorption were studied. Finally, the release of SMZ from MSN and MSN-TETA samples was investigated in a simulated body fluid (pH = 7.4, ionic strength = 150 mM) at T = 37 °C.



Scheme 1. Schematic of MSN-TETA-SMZ as a possible antimicrobial nano-drug.

2. Results

2.1. MSN Structural Characterisation

As described in Section 3.2, MSNs were synthesised using a CTAB template following a method applied in previous work [52]. Subsequently, a Cl-propyl moiety was introduced on the MSN surface to prepare MSN-Cl, which was further treated with TETA to obtain the functionalised MSN-TETA hybrid system. TEM images in Figure 1 show that most MSNs have a spherical or ellipsoidal shape with sizes around 100 nm. The cylindrical channels and the typical hexagonal array of pores (e.g., Figure 1B) can be seen for all porous nanoparticles.

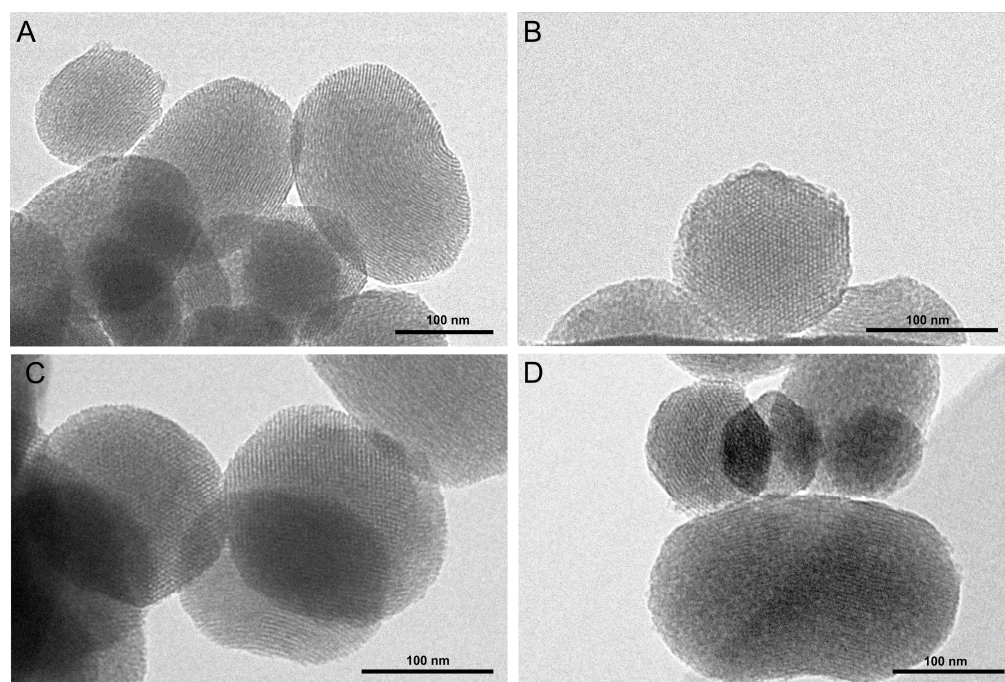


Figure 1. TEM images of MSN sample at different magnifications.

SAXS patterns of MSN, MSN-Cl and MSN-TETA samples showed a strong peak due to the (100) plane and other two weak peaks due to the (110) and (200) planes (Figure 2A). SAXS and TEM analyses confirm the characteristic MSN pattern (based on MCM-41 matrix), which corresponds to an ordered 2D hexagonal structure and p6mm space group [55]. The lattice parameter a is about 47 Å for MSN and the functionalised samples, confirming that the hexagonal array of pores is not affected by surface functionalisation.

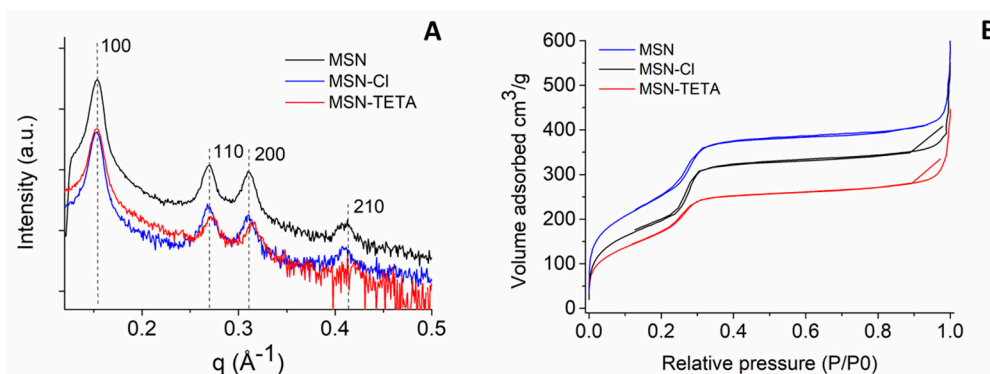


Figure 2. (A) SAXS patterns and (B) Adsorption/desorption N₂ of MSN, MSN-Cl, MSN-TETA samples.

Figure 2B shows the N₂ adsorption/desorption isotherms of MSN, MSN-Cl and MSN-TETA samples. All curves show a sharp increase of N₂ volume adsorption at a relative pressure $P/P_0 = 0.2-0.3$, due to small-sized pores filled by relatively small volumes of N₂. MSN had a BET surface area of 942 m² g⁻¹ that decreased after functionalisation, becoming 744 m² g⁻¹ and 671 m² g⁻¹ for MSN-Cl and MSN-TETA, respectively. The pore volume decreased consistently with TETA functionalisation (Table 1).

Table 1. Surface area (S_{BET}), pore volume (V_p), lattice spacing (a), zeta potential (ζ) and functionalization loadings (L) of MSN, MSN-Cl and MSN-TETA samples.

Sample	^a S_{BET} (m ² g ⁻¹)	^b V_p (cm ³ g ⁻¹)	^c d_p (Å)	^d a (Å)	^e ζ (mV)	^f L (μmol g ⁻¹)
MSN	942	0.78	25	48	-23	-
MSN-Cl	744	0.77	25	47	-8	770
MSN-TETA	671	0.62	24	46	+27	469

^a Specific surface area calculated by the BET equation. ^b Pore volume from the desorption branch calculated at $P/P_0 = 0.99$ by BJH method. ^c Pore diameter calculated by BJH method using desorption branch isotherm. ^d Lattice parameter obtained by SAXS patterns. ^e Zeta potential obtained in suspending particles in distilled water. ^f Functionalisation of propyl-Cl and propyl-TETA loadings calculated by TGA.

The FTIR spectrum of MSN (Figure 3A) shows an intense broad peak at 1060 cm⁻¹ and a less intense peak at 800 cm⁻¹. These typical signals are assigned to the asymmetric and symmetric stretching vibrations of the Si-O-Si bond. Cl-propyl functionalisation is confirmed by the loss of the silanol peak at 976 cm⁻¹, whereas MSN-TETA shows an additional peak at 1642 cm⁻¹ which might be attributed to -NH₂ bending.

The functionalisation of MSN samples was confirmed by thermogravimetric analysis (Figure 3B). Mass losses at $T < 100$ °C are attributed to the loss of humidity. Between 100 and 200 °C, no significant changes in mass are observed for all samples. However, above 200 °C MSN-Cl loses a mass of 8.4% while MSN-TETA loses a mass of 17.3%. This difference (8.9%) is likely due to the TETA moiety. The functionalisation loadings calculated using TG analysis are listed in Table 1.

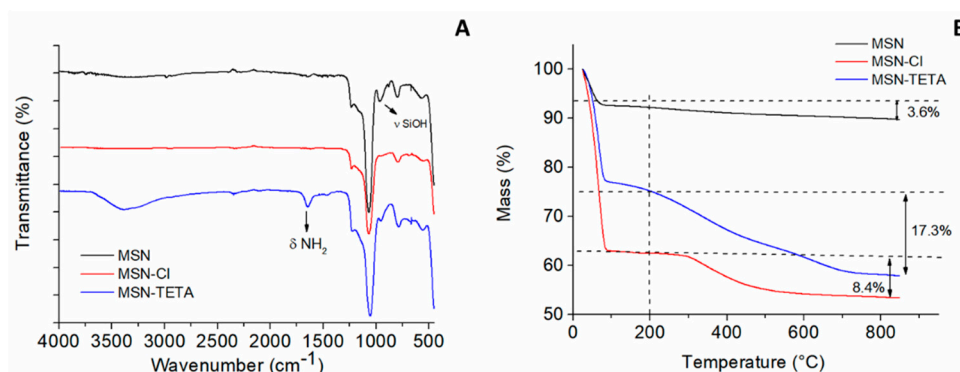


Figure 3. (A) FTIR spectra and (B) Thermogravimetric analysis of MSN, MSN–Cl and MSN–TETA.

In addition, the functionalisation of MSN is also confirmed by zeta potential measurements carried out suspending the different samples in milli-Q water without background salt (Table 1). MSN sample has a negative zeta potential ($\zeta = -23$ mV) due to the dissociation of the silanol groups at $\text{pH} > 2-3$ [56]. The sample MSN-Cl has a less negative zeta potential ($\zeta = -8$ mV) likely since replacement of most silanols with Cl-PTES has occurred. MSN-TETA system displays a positive zeta potential ($\zeta = +27$ mV) due to the functionalisation with triethylenetetramine groups, which are protonated in aqueous solution.

2.2. SMZ Adsorption on MSN and MSN-TETA

SMZ drug was then adsorbed on MSN and MSN-TETA samples. SMZ presence on MSN is qualitatively confirmed by FTIR spectra (Figure 4A). The bands at 3447 e 3343 cm^{-1} are assigned to the symmetric and asymmetric stretching of aromatic $-\text{NH}_2$ [57], while that at 3220 cm^{-1} is assigned to stretching of the S-N bond in SO_2NH . The other two peaks, associated with O=S=O stretching (1450 e 1556 cm^{-1}), and O=S=O bending (568 a 487 cm^{-1}), confirm the loading of the drug on both MSN and MSN-TETA samples, respectively. A mass loss at $T > 200$ $^\circ\text{C}$ is observed for MSN-SMZ (12.3%) and MSN-TETA-SMZ (33.7%). Mass loss is entirely assigned to SMZ for MSN, while in the case of MSN-TETA, the loss of 33.7% can be only in part due to SMZ, since the decomposition of propyl-TETA moiety (17.3%) occurs in the same temperature range. These mass loss data, considered the contribution of the TETA moiety, correspond to a SMZ loading of 163 mg g^{-1} and 123 mg g^{-1} for MSN-TETA and MSN, respectively.

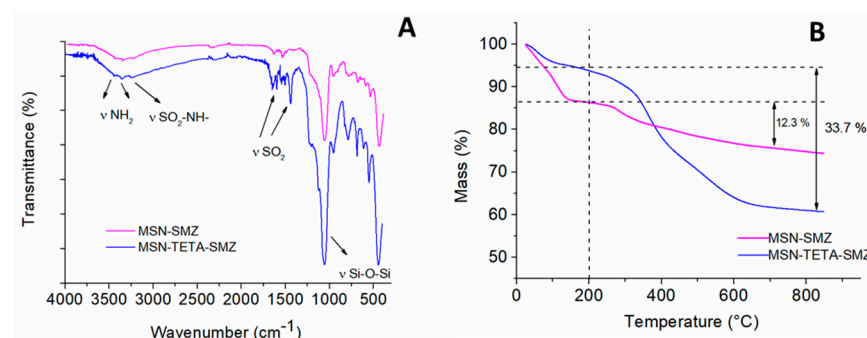


Figure 4. (A) FT-IR spectra (B) TGA of MSN-SMZ and MSN-TETA-SMZ.

2.3. Adsorption Kinetics of Sulphamethizole on MCM-41 and MCM-41-TETA

The adsorption kinetics of SMZ on MSN and MSN-TETA was then studied. The adsorbed amount (q_t , mg g^{-1}) of SMZ drug as a function of the contact time is shown in Figure 5A. Both samples show a rapid q_t increase within the first phase of adsorption reaching equilibrium after approximately 5 h. Data were analysed with pseudo-first-order (Figure 5B) and pseudo-second-order (Figure 5C) kinetic models [52,58]. The low R^2 of the pseudo-first order model suggests that this model is not suitable to describe SMZ

adsorption. On the contrary, the pseudo-second order model fits the experimental data quite well ($R^2 = 0.99$ for both samples). This is also confirmed by the adsorbed amounts at equilibrium (q_{eq}) of the experimental data compared against the data calculated by the pseudo-second order model. Indeed, calculated q_{eq} were 216.2 and 332.2 mg g^{-1} for MSN and MSN-TETA, respectively, with the experimental values being 232.9 and 389.1 mg g^{-1} for MSN and MSN-TETA, respectively (see Table 2). This finding agrees with Fukahori et al. who studied the adsorption kinetics of SMZ on zeolites at pH 3.8 [59].

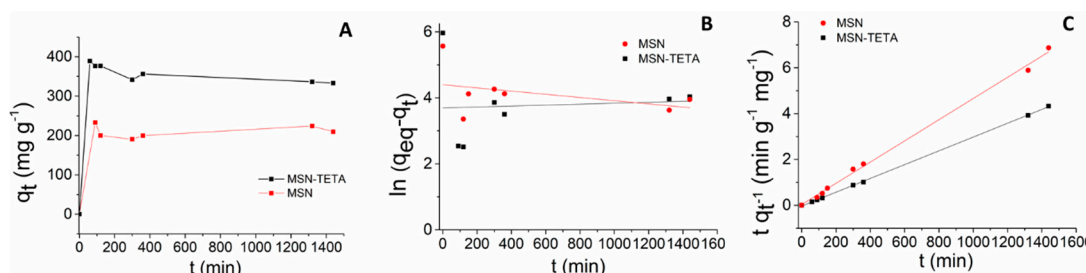


Figure 5. (A) Adsorption kinetics of SMZ on MSN and MSN-TETA fitted with (B) pseudo-first order and (C) pseudo-second order models.

Table 2. Kinetic parameters for SMZ adsorption on MSN and MSN-TETA.

Sample	Pseudo-First Order			Pseudo-Second Order			
	q_{eq}^{exp} (mg g^{-1})	k' (min^{-1})	q_{eq}^{calc} (mg g^{-1})	R^2	k'' ($\text{g mg}^{-1} \text{min}^{-1}$)	q_{eq}^{calc} (mg g^{-1})	R^2
MSN-SMZ	232.9	4.8×10^{-4}	81.3	0.17	6.4×10^{-4}	216.2	0.99
MSN-TETA-SMZ	389.1	1.4×10^{-4}	40.2	0.005	2.9×10^{-4}	332.2	0.99

2.4. Adsorption Isotherms of Sulphamethizole on MCM-41 and MCM-41-TETA

The adsorption isotherms of SMZ on MSN and MSN-TETA samples at 298 K were then determined. Figure 6 shows the SMZ adsorbed amount (q_{eq} , $\text{mg}_{\text{SMZ}}/\text{g}_{\text{MSN/MSN-TETA}}$) vs. its equilibrium concentration in the adsorbing solution (C_{eq} , $\text{mg}_{\text{SMZ}}/\text{mL}$). The highest SMZ loadings were obtained with the functionalised MSN-TETA, corroborating the figures reported above from TGA (Figure 4). The experimental data were analysed using Freundlich, Temkin and Langmuir models as described in the experimental section [60,61].

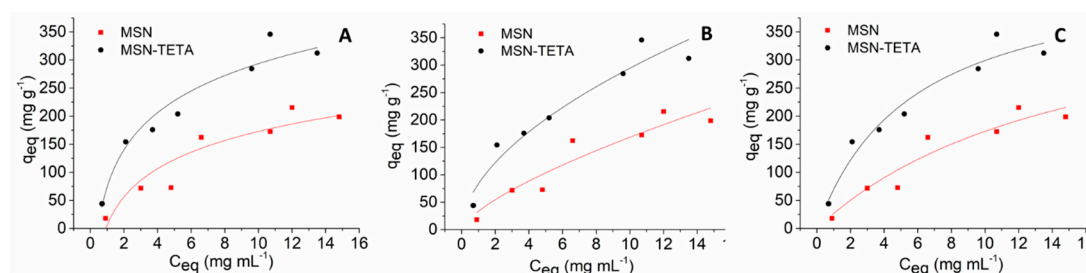


Figure 6. Adsorption isotherms (298 K) of SMZ on MSN and MSN-TETA fitted with Temkin (A), Freundlich (B), and Langmuir (C) models.

Temkin (Figure 6A) and Freundlich (Figure 6B) models show a low correlation coefficient for MSN samples ($R^2 = 0.85$ and $R^2 = 0.88$, respectively). Langmuir (Figure 6C) model shows the best correlation coefficient for both MSN and MSN-TETA samples ($R^2 = 0.90$ and 0.95 , respectively) (Table 3). This suggests the formation of SMZ monolayer on both MSN and MSN-TETA, although a clear plateau is not reached within the explored concentration range. However, higher SMZ concentrations in the adsorbing solution could not be used because of solubility limitations. Jia et al. studied the adsorption behaviour of sulphadiazine

(SDZ), sulphamethoxazole (SMX), and sulphadoxine (SDX) on a MIL-101(Cr)@GO metal organic framework [62]. They found a maximum loading capacity of 135.1 mg g⁻¹ for SDZ, 101.0 mg g⁻¹ for SMX and 119.1 mg g⁻¹ for SDX. The estimated maximum monolayer coverage of SMZ found in our work is higher for MSN-TETA (465.3 mg g⁻¹) than for MSN (442.0 mg g⁻¹). In our experimental conditions, the highest adsorbed amount of SMZ is 345.8 mg g⁻¹ for MSN-TETA and 215.4 mg g⁻¹ for MSN samples (Figure 6). Interestingly, a significant higher loading is found for MSN-TETA system compared with MSN although functionalisation decreases the surface area available for SMZ adsorption, as demonstrated by N₂-isotherms experiments. The higher SMZ adsorption obtained with MSN-TETA carrier might be due to the establishment of favourable interactions between the adsorbent and the adsorbate. Indeed, SMZ molecules are in anionic form already at pH > 5.3 (pI ~ 4 due to pKa₁ = 2.1 ± 0.2 and pKa₂ = 5.3 ± 0.2) [63]. It may be suggested that TETA groups, which make MSN-TETA surface positively charged, attract the negatively charged SMZ molecules, thus favouring a higher loading than that of bare MSN, as a result of electrostatic interactions. Similar behaviour was previously observed for ampicillin [64], sulphasalazine [65] and nucleic acids [66].

Table 3. Adsorption isotherm parameters for SMZ on MSN and MSN-TETA.

Sample	Temkin			Freundlich			Langmuir			
	q _{exp} (mg g ⁻¹)	b _t (J mol ⁻¹)	A _T (mL mg ⁻¹)	R ²	K _F (L mg ⁻¹)	n	R ²	K _L (L mg ⁻¹)	q _{max} (mg g ⁻¹)	R ²
MSN-SMZ	215.4	37.5	1.1	0.85	33.5	1.4	0.88	0.08	442.0	0.90
MSN-TETA-SMZ	345.8	25.7	2.1	0.95	83.7	1.8	0.94	0.18	465.3	0.95

2.5. In Vitro Release of SMZ

In vitro release of SMZ from MSN and MSN-TETA carriers was then studied. The maximal released amount (A_{max}%) of SMZ was 69.8% and 42.7% for MSN and MSN-TETA, respectively (Table 4). The kinetic release constant k₁ has a very high value for bare MSN consistent with a burst release of the drug. In contrast, SMZ is released more slowly from MSN-TETA (k = 3.04 h⁻¹), thus indicating that TETA functionalisation slows down drug release (Figure 7). The same attractive interactions that promote a higher loading of SMZ on MSN-TETA surface are likely responsible of the lower and slower drug release. The maximal amounts of released drug correspond to an SMZ concentration in the release solution of 171 µg mL⁻¹ and 102 µg mL⁻¹ for MSN and MSN-TETA, respectively. It is interesting to compare these concentrations with the dose of SMZ, or other similar drugs, in biological fluids. Sulfamethoxazole has a chemical structure similar to that of SMZ (an oxazole substitutes the thiadiazole moiety) and is also used in urinary tract infections as bacteriostatic in combination with trimethoprim [67]. After 8 h of oral administration, sulphamethoxazole reaches in an adult (24–34 years old) a blood concentration that varies from 98 to 128 µg mL⁻¹ [68]. The active therapeutical sulfamethoxazole is counted in serum rather than in blood, with an optimal peak concentration of 100–150 µg/mL [69,70]. These values are comparable with the maximum SMZ concentration released by MSN and MSN-TETA found in the present work.

Table 4. Kinetic parameters for SMZ release from MSN and MSN-TETA.

Samples	k ₁ (h ⁻¹)	A _{max} (%)	A _{max} (µg mL ⁻¹)	R ²
MSN-SMZ	136	69.8	171	0.98
MSN-TETA-SMZ	3.04	42.7	102	0.96

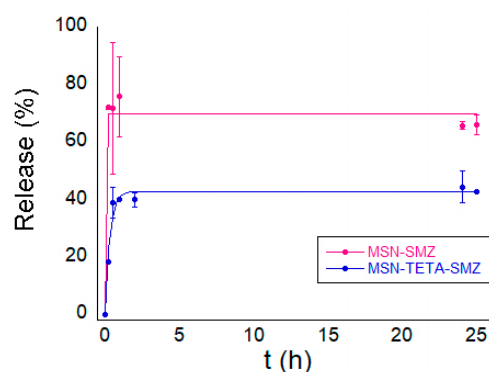


Figure 7. In vitro SMZ release of MSN and MSN-TETA.

3. Materials and Methods

3.1. Materials

Hexadecyltrimethylammonium bromide CTAB (>99%), tetraethoxysilane TEOS (98%), anhydrous toluene (99.8%), triethylenetetramine TETA ($\geq 97\%$), NaH_2PO_4 (99%), Na_2HPO_4 (99%), NaCl, NaOH, 3-chloropropyltrimethoxysilane CPTMS ($\geq 97\%$), toluene, ammonium nitrate NH_4NO_3 , sulphamethizole (99%) and dimethylformamide (DMF $\geq 99.9\%$), were purchased from Sigma Aldrich (Milano, Italy). Ethanol (99.8%) was provided by Honeywell.

3.2. Synthesis and Functionalisation of MSNs

MSN samples were synthesised as described elsewhere [64]. Briefly, 3.5 mL of NaOH (2 M) was added under stirring to 480 mL of H_2O with 1 g of CTAB avoiding bubbles formation. The mixture was immersed in an oil bath at $80\text{ }^\circ\text{C}$ with mild stirring. Before slowly adding 5 mL of TEOS with a syringe, stirring was increased up to 400 rpm. The reaction mixture was then kept at $80\text{ }^\circ\text{C}$ for 2 h. The product was then collected, filtered and washed with water and ethanol. CTAB extraction was carried out by suspending 3 g of product in 1 L of a EtOH/ H_2O (95:5 v/v) solution containing NH_4NO_3 10 g L^{-1} , kept for 2 h at $80\text{ }^\circ\text{C}$. TETA functionalisation was conducted by a method similar to that reported in the literature for other silica materials [71]. Briefly, 0.7 mL of CPTMS was added to 1 g of MSN suspended in 25 mL of anhydrous toluene. The reaction mixture was left overnight under reflux at $110\text{ }^\circ\text{C}$. The obtained MSN-Cl was filtered, washed with toluene, ethanol and water and dried at $40\text{ }^\circ\text{C}$. A mass of 1.12 g of TETA were solubilised in 2 mL of DMF under heating for 1 or 2 min at $\sim 30\text{ }^\circ\text{C}$. A mass of 1 g of MSN-Cl was then suspended in the TETA solution in DMF and left under stirring for 25 h at $110\text{ }^\circ\text{C}$.

3.3. Physico-Chemical Characterisations

MSN samples were characterised through transmission electron microscopy (TEM), small-angle X-rays scattering (SAXS), N_2 adsorption–desorption isotherms, Fourier-transform infrared spectroscopy (FTIR), thermogravimetric analysis (TGA) and electrophoretic light scattering (ELS, zeta potential). TEM images were obtained on a JEOL 100S microscope. Small-angle X-ray scattering (SAXS) patterns were recorded with a S3-MICRO SWAXS camera system (HECUS X-ray Systems, Graz, Austria). The scattering patterns were recorded for 1 h. Textural analysis was carried out on an ASAP 2020 instrument, by determining the N_2 adsorption/desorption isotherms at 77 K. Before analysis, MSN samples were heated at $250\text{ }^\circ\text{C}$ at a rate of $1\text{ }^\circ\text{C}/\text{min}$ under vacuum for 12 h. MSN-Cl, MSN-TETA and MSN-TETA-SMZ were heated at $25\text{ }^\circ\text{C}$ at the rate of $1\text{ }^\circ\text{C}/\text{min}$ under vacuum for 12 h. The Brunauer–Emmett–Teller (BET) [72] and Barrett–Joyner–Halenda (BJH) [73] methods were used to calculate surface area, pore volume and pore size distribution (from the desorption branch of N_2 isotherm). FTIR studies were conducted with a Brüker Tensor 27 FTIR spectrometer equipped with a diamond-ATR accessory in the $4000\text{--}400\text{ cm}^{-1}$ range with a number of 128 scans at a resolution of 2 cm^{-1} . TGA measurements were carried out in the T range $25\text{--}850\text{ }^\circ\text{C}$ (heating rate = $10\text{ }^\circ\text{C}/\text{min}$), and under oxygen flow by means of a Perkin Elmer TGA7/DSC7.

3.4. Adsorption Kinetic Models

Kinetics of SMZ adsorption on MSN and MSN-TETA was determined [60] by suspending 10 mg of MSN or MSN-TETA in 1 mL of a SMZ solution (10 mg mL⁻¹) in a mixture of EtOH/H₂O 60:40, and left under rotation for 60, 100, 300, 360, 1320 and 1440 min at 25 °C. The supernatant was then assayed in a quartz cuvette taking 3 µL of solution and diluting it in 3 mL of a EtOH/H₂O 60:40 solution. At different times, the supernatant of each sample was analysed through an Agilent Cary 60 UV-Vis spectrophotometer at 280 nm. The concentration of SMZ in the adsorption solution was calculated through a calibration curve (concentration range 0.5–20 mg mL⁻¹). The residual SMZ concentration evaluated by UV-Vis and the corresponding adsorbed amount q_t (mg g⁻¹) was plotted vs. time. Kinetics measurements were analysed by different kinetic models named as:

Pseudo-first-order (differential form) [74]

$$\frac{dq_t}{dt} = k'(q_{eq} - q_t) \quad (1)$$

for which the linearised form is expressed as:

$$\ln(q_{eq} - q_t) = \ln q_{eq} - k't \quad (2)$$

q_{eq} is the adsorbed quantity of adsorbate at the equilibrium and q_t the adsorbed quantity (mg g⁻¹) at time t (min), k' is the pseudo first order kinetic constant expressed in min⁻¹.

Alternatively, the pseudo-second-order model was used [75]:

$$\frac{dq_t}{dt} = k''(q_{eq} - q_t)^2 \quad (3)$$

for which the linearised form is expressed as:

$$\frac{t}{q_t} = \frac{1}{(k''q_{eq}^2)} + \frac{t}{q_{eq}} \quad (4)$$

where k'' is the pseudo-second-order kinetic constant (g mg⁻¹ min⁻¹).

3.5. Adsorption Isotherms

Adsorption isotherm studies were carried out by suspending 10 mg of MSN or MSN-TETA in 1 mL of a solution of SMZ dissolved in a EtOH/H₂O 60:40 mixture at different concentrations (from 1.1 to 16.7 mg mL⁻¹) under constant rotation for 24 h at 25 °C. The SMZ equilibrium concentration in the supernatant, obtained by centrifugation for 2 min at 1500 rpm, was then assayed by UV-Vis spectroscopy. A volume of 3 µL of the supernatant was diluted in 3 mL of a solution EtOH/H₂O 60:40 in a quartz cuvette. The absorbance of SMZ solutions was measured through an Agilent Cary 60 UV-Vis spectrophotometer at 280 nm, and the concentration of SMZ in the adsorption solution was calculated with the appropriate calibration curve (concentration range 0.5–20 mg mL⁻¹). Adsorption data were fitted through Freundlich, Temkin, and Langmuir models.

Freundlich model describes the adsorption isotherm as [76]:

$$q_{eq} = K_F C_{eq}^{1/n} \quad (5)$$

In which, q_{eq} is the adsorbed amount (mg of adsorbate/g of adsorbent), C_{eq} (mg mL⁻¹) is the equilibrium concentration, K_F (support capacity, L mg⁻¹) is Freundlich constant and n (heterogeneity factor) is a dimensionless parameter that describes the heterogeneous adsorbent surface. Both empirical parameters are specific for adsorbent-adsorbate interactions at a specific temperature. With heterogeneous adsorption sites, a formation of multilayer is to be expected.

The Langmuir model [77]:

$$q_{eq} = \frac{q_{max}K_L C_{eq}}{1 + K_L C_{eq}} \quad (6)$$

where, q_{eq} is the adsorbed amount at the equilibrium (mg g^{-1}), q_{max} is the maximum cover capacity (mg g^{-1}), K_L is Langmuir constant (L mg^{-1}) and C_{eq} (mg mL^{-1}) is the equilibrium concentration. Langmuir model assumes that the adsorbent is homogeneous, and all the sites are equivalent, and only a monolayer of molecules is permitted.

Temkin model [78]:

$$q_{eq} = \frac{RT}{b_T} \ln(A_T C_{eq}) \quad (7)$$

where, b_T is the Temkin constant (J mol^{-1}), R is ideal gas constant ($\text{J mol}^{-1} \text{K}^{-1}$), T is the absolute temperature (K), A_T is the isotherm equilibrium binding constant (mL mg^{-1}) and C_{eq} (mg mL^{-1}) is the equilibrium concentration. According to Temkin model, the indirect effect of adsorbent–adsorbate interactions matters. It assumes that the adsorption enthalpy of adsorbed drug is due to an increase in surface covering.

3.6. Kinetics of SMZ Release

SMZ release kinetic studies were carried out suspending 50 mg of MSN-SMZ or MSN-TETA-SMZ samples in different vessels containing 50 mL of 100 mM phosphate buffer pH 7.4 NaCl 150 mM (PBS) at 37 °C. To analyse the SMZ release, other withdrawals were made at different times within 25 h. Each withdrawal was made of 2 mL, and the same amount of liquid was reconstituted with PBS buffer in each vessel to maintain “sink conditions” [79]. Results were analysed with an appropriate calibration curve and reported in percentage by the equation [80]:

$$\frac{M_t}{M_0} (\%) = A_{max} (1 - e^{-kt}) \quad (8)$$

where M_t (mg) is drug mass at time of the withdrawal t , M_0 (mg) is the mass of drug loaded, A_{max} is the maximum drug release and k_1 (h^{-1}) is the release constant rate.

4. Conclusions

Herein, a new DDS based on SMZ loaded on MSN and MSN-TETA is reported. TEM and SAXS structural characterisations confirmed the successful synthesis of MSN having the typical hexagonal structure. N_2 -isotherms of MSN showed a surface area of $942 \text{ m}^2 \text{ g}^{-1}$ that, as expected, and decreased because of material functionalisation. TGA and FTIR techniques were used to characterise functionalised and post-adsorption samples, highlighting a higher drug loading with MSN-TETA (up to 345 mg g^{-1}), despite its lower surface area value ($671 \text{ m}^2 \text{ g}^{-1}$), with respect to that of MSN (up to 215.4 mg g^{-1}). SMZ adsorption kinetics on both MSN and MSN-TETA was consistent with a pseudo-second-order model, whereas the adsorption isotherms were consistent with the Langmuir model. The SMZ release of both materials was studied achieving up to 69.8% ($171 \mu\text{g mL}^{-1}$) for MSN and 42.7% for MSN-TETA ($102 \mu\text{g mL}^{-1}$). The latter concentration is very similar to the concentration of similar drugs measured in the blood. Interestingly, SMZ release was slower from MSN-TETA ($k_1 = 3.04 \text{ h}^{-1}$) compared with MSN ($k_1 = 136 \text{ h}^{-1}$). These findings highlight the importance of the establishment of suitable drug–carrier interactions. Indeed, as observed here, the positive charged functionalisation with TETA moieties may favour the interactions with the negatively charged SMZ rather than the negatively charged MSN surface. The attractive electrostatic interaction between SMZ and MSN-TETA surface is responsible for a higher loading and a slower release compared with the SMZ-MSN pair. The present DDS, based on SMZ loaded on MSN-TETA obtained here, could be potentially used against Gram negative bacteria such as *E. coli* to treat urinary tract infections. The therapeutic antibacterial activity of the promising DDS will deserve to be tested in a future work.

Author Contributions: Conceptualization, A.S. and C.C.; methodology, investigation, N.S. and C.C.; data curation; writing—original draft preparation, C.C., N.S., A.P., M.P., M.M. and A.S.; writing—review and editing, C.C., N.S., A.P., M.P., M.M. and A.S., funding acquisition, A.S. All authors have read and agreed to the published version of the manuscript.

Funding: Financial support from FIR 2020, Fondazione di Sardegna (FdS, F72F20000230007), and from Regione Autonoma della Sardegna (RASSR79857) are gratefully acknowledged. Author C.C. thanks MIUR (PON-AIM Azione I.2-DD n. 407-27.02.2018, AIM1890410-2).

Institutional Review Board Statement: Not applicable.

Informed Consent Statement: Not applicable.

Data Availability Statement: Not applicable.

Acknowledgments: We acknowledge the CeSAR (Centro Servizi di Ateneo per la Ricerca) of the University of Cagliari, Italy for access to a JEM 1400 Plus TEM microscope. Drew F. Parsons is acknowledged for his valuable help with the revision of the manuscript.

Conflicts of Interest: The authors declare no conflict of interest. The funders had no role in the study's design; in the collection, analyses, or interpretation of data; in the writing of the manuscript, or in the decision to publish the results.

References

1. Park, K. Controlled drug delivery systems: Past forward and future back. *J. Control. Release* **2014**, *190*, 3–8. [[CrossRef](#)]
2. Manzano, M.; Vallet-Regí, M. New developments in ordered mesoporous materials for drug delivery. *J. Mater. Chem.* **2010**, *20*, 5593–5604. [[CrossRef](#)]
3. Piludu, M.; Medda, L.; Monduzzi, M.; Salis, A. Gold Nanoparticles: A Powerful Tool to Visualize Proteins on Ordered Mesoporous Silica and for the Realization of Theranostic Nanobioconjugates. *Int. J. Mol. Sci.* **2018**, *19*, 1991. [[CrossRef](#)] [[PubMed](#)]
4. Manzano, M.; Vallet-Regí, M. Mesoporous silica nanoparticles for drug delivery. *Adv. Funct. Mater.* **2020**, *30*, 1902634. [[CrossRef](#)]
5. Hudson, S.P.; Padera, R.F.; Langer, R.; Kohane, D.S. The biocompatibility of mesoporous silicates. *Biomaterials* **2008**, *29*, 4045–4055. [[CrossRef](#)] [[PubMed](#)]
6. Yang, Y.; Zhao, W.; Tan, W.; Lai, Z.; Fang, D.; Jiang, L.; Zuo, C.; Yang, N.; Lai, Y. An Efficient Cell-Targeting Drug Delivery System Based on Aptamer-Modified Mesoporous Silica Nanoparticles. *Nanoscale Res. Lett.* **2019**, *14*, 1–10. [[CrossRef](#)] [[PubMed](#)]
7. Thomas, R.G.; Surendran, S.P.; Jeong, Y.Y. Tumor Microenvironment-Stimuli Responsive Nanoparticles for Anticancer Therapy. *Front. Mol. Biosci.* **2020**, *7*. [[CrossRef](#)] [[PubMed](#)]
8. Chen, X.; Cheng, X.; Soeriyadi, A.; Sagnella, S.M.; Lu, X.; Scott, J.; Lowe, S.B.; Kavallaris, M.; Gooding, J.J. Stimuli-responsive functionalized mesoporous silica nanoparticles for drug release in response to various biological stimuli. *Biomater. Sci.* **2014**, *2*, 121–130. [[CrossRef](#)]
9. Vallet-Regí, M.; Rámila, A.; DEL Real, R.P.; Perez-Pariente, J. A New Property of MCM-41: Drug Delivery System. *Chem. Mater.* **2001**, *13*, 308–311. [[CrossRef](#)]
10. Ambroggi, V.; Perioli, L.; Pagano, C.; Latterini, L.; Marmottini, F.; Ricci, M.; Rossi, C. MCM-41 for furosemide dissolution improvement. *Microporous Mesoporous Mater.* **2012**, *147*, 343–349. [[CrossRef](#)]
11. Varache, M.; Bezverkhyy, I.; Saviot, L.; Bouyer, F.; Baras, F.; Bouyer, F. Optimization of MCM-41 type silica nanoparticles for biological applications: Control of size and absence of aggregation and cell cytotoxicity. *J. Non Cryst. Solids* **2015**, *408*, 87–97. [[CrossRef](#)]
12. Popova, T.; Voycheva, C.; Tzankov, B. Study on the influence of technological factors on drug loading of poorly water-soluble drug on MCM-41 mesoporous carrier. *Pharmacia* **2020**, *67*, 351–356. [[CrossRef](#)]
13. Roik, N.; Belyakova, L.A.; Dziuzko, M.O. Adsorption of antitumor antibiotic doxorubicin on MCM-41-type silica surface. *Adsorpt. Sci. Technol.* **2017**, *35*, 86–101. [[CrossRef](#)]
14. He, Q.; Shi, J. MSN Anti-Cancer Nanomedicines: Chemotherapy Enhancement, Overcoming of Drug Resistance, and Metastasis Inhibition. *Adv. Mater.* **2014**, *26*, 391–411. [[CrossRef](#)] [[PubMed](#)]
15. LaBauve, A.E.; Rinker, T.E.; Noureddine, A.; Serda, R.E.; Howe, J.Y.; Sherman, M.B.; Rasley, A.; Brinker, C.J.; Sasaki, D.Y.; Negrete, O.A. Lipid-Coated Mesoporous Silica Nanoparticles for the Delivery of the ML336 Antiviral to Inhibit Encephalitic Alphavirus Infection. *Sci. Rep.* **2018**, *8*, 1–13. [[CrossRef](#)] [[PubMed](#)]
16. Mohseni, M.; Gilani, K.; Mortazavi, S.A. Preparation and Characterization of Rifampin Loaded Mesoporous Silica Nanoparticles as a Potential System for Pulmonary Drug Delivery. *Iran. J. Pharm. Res.* **2015**, *14*, 27–34. [[CrossRef](#)]
17. Ganesh, M.; Gil Lee, S. Synthesis, Characterization and Drug Release Capability of New Cost Effective Mesoporous Silica Nano Particle for Ibuprofen Drug Delivery. *Int. J. Control. Autom.* **2013**, *6*, 207–216. [[CrossRef](#)]
18. Alexa, I.F.; Ignat, M.; Popovici, R.F.; Timpu, D.; Popovici, E. In vitro controlled release of antihypertensive drugs intercalated into unmodified SBA-15 and MgO modified SBA-15 matrices. *Int. J. Pharm.* **2012**, *436*, 111–119. [[CrossRef](#)] [[PubMed](#)]

19. González, B.; Colilla, M.; Díez, J.; Pedraza, D.; Guembe, M.; Izquierdo-Barba, I.; Vallet-Regí, M. Mesoporous silica nanoparticles decorated with polycationic dendrimers for infection treatment. *Acta Biomater.* **2018**, *68*, 261–271. [[CrossRef](#)]
20. Martínez-Carmona, M.; Izquierdo-Barba, I.; Colilla, M.; Vallet-Regí, M. Concanavalin A-targeted mesoporous silica nanoparticles for infection treatment. *Acta Biomater.* **2019**, *96*, 547–556. [[CrossRef](#)] [[PubMed](#)]
21. Salis, A.; Fanti, M.; Medda, L.; Nairi, V.; Cugia, F.; Piludu, M.; Sogos, V.; Monduzzi, M. Mesoporous Silica Nanoparticles Functionalized with Hyaluronic Acid and Chitosan Biopolymers. Effect of Functionalization on Cell Internalization. *ACS Biomater. Sci. Eng.* **2016**, *2*, 741–751. [[CrossRef](#)]
22. Nairi, V.; Magnolia, S.; Piludu, M.; Nieddu, M.; Caria, C.A.; Sogos, V.; Vallet-Regí, M.; Monduzzi, M.; Salis, A. Mesoporous silica nanoparticles functionalized with hyaluronic acid. Effect of the biopolymer chain length on cell internalization. *Colloids Surf. B Biointerfaces* **2018**, *168*, 50–59. [[CrossRef](#)]
23. Nairi, V.; Medda, S.; Piludu, M.; Casula, M.F.; Vallet-Regí, M.; Monduzzi, M.; Salis, A. Interactions between bovine serum albumin and mesoporous silica nanoparticles functionalized with biopolymers. *Chem. Eng. J.* **2018**, *340*, 42–50. [[CrossRef](#)]
24. Mitchell, M.J.; Billingsley, M.M.; Haley, R.M.; Wechsler, M.E.; Peppas, N.A.; Langer, R. Engineering precision nanoparticles for drug delivery. *Nat. Rev. Drug Discov.* **2021**, *20*, 101–124. [[CrossRef](#)] [[PubMed](#)]
25. Vallet-Regí, M.; González, B.; Izquierdo-Barba, I. Nanomaterials as Promising Alternative in the Infection Treatment. *Int. J. Mol. Sci.* **2019**, *20*, 3806. [[CrossRef](#)] [[PubMed](#)]
26. Narayan, R.; Nayak, U.Y.; Raichur, A.M.; Garg, S. Mesoporous Silica Nanoparticles: A Comprehensive Review on Synthesis and Recent Advances. *Pharmacia* **2018**, *10*, 118. [[CrossRef](#)]
27. Lu, J.; Li, Z.; Zink, J.I.; Tamanoi, F. In vivo tumor suppression efficacy of mesoporous silica nanoparticles-based drug-delivery system: Enhanced efficacy by folate modification. *Nanomed. Nanotechnol. Biol. Med.* **2012**, *8*, 212–220. [[CrossRef](#)] [[PubMed](#)]
28. Lee, E.C.; Nguyen, C.T.H.; Strounina, E.; Davis-Poynter, N.; Ross, B.P. Structure–Activity Relationships of GAG Mimetic-Functionalized Mesoporous Silica Nanoparticles and Evaluation of Acyclovir-Loaded Antiviral Nanoparticles with Dual Mechanisms of Action. *ACS Omega* **2018**, *3*, 1689–1699. [[CrossRef](#)] [[PubMed](#)]
29. Gounani, Z.; Asadollahi, M.A.; Meyer, R.L.; Arpanaei, A. Loading of polymyxin B onto anionic mesoporous silica nanoparticles retains antibacterial activity and enhances biocompatibility. *Int. J. Pharm.* **2018**, *537*, 148–161. [[CrossRef](#)] [[PubMed](#)]
30. Blair, J.; Webber, M.A.; Baylay, A.J.; Ogbolu, D.O.; Piddock, L.J.V. Molecular mechanisms of antibiotic resistance. *Nat. Rev. Microbiol.* **2015**, *13*, 42–51. [[CrossRef](#)] [[PubMed](#)]
31. Ledingham, K. Using a cultural contexts of health approach to address the challenge of antibiotic resistance. *Eur. J. Public Health* **2019**, *29*. [[CrossRef](#)]
32. Alanis, A.J. Resistance to Antibiotics: Are We in the Post-Antibiotic Era? *Arch. Med Res.* **2005**, *36*, 697–705. [[CrossRef](#)] [[PubMed](#)]
33. Labrière, R.; Sona, A.J.; Turos, E. Anti-Methicillin-Resistant *Staphylococcus aureus* Nanoantibiotics. *Front. Pharmacol.* **2019**, *10*, 1121. [[CrossRef](#)] [[PubMed](#)]
34. McManus, M.C. Mechanisms of bacterial resistance to antimicrobial agents. *Am. J. Health Pharm.* **1997**, *54*, 1420–1433. [[CrossRef](#)] [[PubMed](#)]
35. Parasca, O.M.; Gheată, F.; Pânzariu, A.; Geangalău, I.; Profire, L. Importance of Sulfonamide Moiety in Current and Future Therapy. *Rev. Med. Chir. Soc. Medici Nat. Iași* **2013**, *117*, 558–564.
36. Fernández-Villa, D.; Aguilar, M.R.; Rojo, L. Folic Acid Antagonists: Antimicrobial and Immunomodulating Mechanisms and Applications. *Int. J. Mol. Sci.* **2019**, *20*, 4996. [[CrossRef](#)] [[PubMed](#)]
37. Brown, G.M. The Biosynthesis of Folic Acid. *J. Biol. Chem.* **1962**, *237*, 536–540. [[CrossRef](#)]
38. Claudel, M.; Schwarte, J.V.; Fromm, K.M. New Antimicrobial Strategies Based on Metal Complexes. *Chemistry* **2020**, *2*, 849–899. [[CrossRef](#)]
39. Dai, T.; Huang, Y.; Sharma, S.K.; Hashmi, J.T.; Kurup, D.B.; Hamblin, M.R. Topical antimicrobials for burn wound infections. *Recent Pat. Anti Infect. Drug Discov.* **2010**, *5*, 124–151. [[CrossRef](#)]
40. Peddie, B.A.; Little, P.J.; Peddle, B.A. Sulphamethizole in urinary tract infections. *J. Antimicrob. Chemother.* **1979**, *5*, 195–200. [[CrossRef](#)]
41. Ghedini, E.; Pizzolitto, C.; Albore, G.; Menegazzo, F.; Signoretto, M.; Operti, L.; Cerrato, G. Sulfadiazine-based drug delivery systems prepared by an effective sol-gel process. *J. Sol Gel Sci. Technol.* **2017**, *83*, 618–626. [[CrossRef](#)]
42. Águila-Rosas, J.; Quirino-Barreda, C.T.; Leyva-Gómez, G.; González-Zamora, E.; Ibarra, I.A.; Lima, E. Sulfadiazine hosted in MIL-53(Al) as a biocide topical delivery system. *RSC Adv.* **2020**, *10*, 25645–25651. [[CrossRef](#)]
43. Jangra, S.; Devi, S.; Tomer, V.K.; Chhokar, V.; Duhan, S. Improved antimicrobial property and controlled drug release kinetics of silver sulfadiazine loaded ordered mesoporous silica. *J. Asian Ceram. Soc.* **2016**, *4*, 282–288. [[CrossRef](#)]
44. Giret, S.; Man, M.W.C.; Carcel, C. Mesoporous-Silica-Functionalized Nanoparticles for Drug Delivery. *Chem. A Eur. J.* **2015**, *21*, 13850–13865. [[CrossRef](#)]
45. Musso, G.E.; Bottinelli, E.; Celi, L.R.; Magnacca, G.; Berlier, G. Influence of surface functionalization on the hydrophilic character of mesoporous silica nanoparticles. *Phys. Chem. Chem. Phys.* **2015**, *17*, 13882–13894. [[CrossRef](#)]
46. Montalvo-Quirós, S.; Vallet-Regí, M.; Palacios, A.; Anguita, J.; Prados-Rosales, R.C.; González, B.; Luque-García, J.L. Mesoporous Silica Nanoparticles as a Potential Platform for Vaccine Development against Tuberculosis. *Pharmaceutics* **2020**, *12*, 1218. [[CrossRef](#)]
47. Fulaz, S.; Devlin, H.; Vitale, S.; Quinn, L.; O’Gara, J.P.; Casey, E. Tailoring Nanoparticle-Biofilm Interactions to Increase the Efficacy of Antimicrobial Agents Against *Staphylococcus aureus*. *Int. J. Nanomed.* **2020**, *ume 15*, 4779–4791. [[CrossRef](#)]

48. Zaharudin, N.S.; Isa, E.D.M.; Ahmad, H.; Rahman, M.B.A.; Jumbri, K. Functionalized mesoporous silica nanoparticles templated by pyridinium ionic liquid for hydrophilic and hydrophobic drug release application. *J. Saudi Chem. Soc.* **2020**, *24*, 289–302. [[CrossRef](#)]
49. Niu, J.; Tang, G.; Tang, J.; Yang, J.; Zhou, Z.; Gao, Y.; Chen, X.; Tian, Y.; Li, Y.; Li, J.; et al. Functionalized Silver Nanocapsules with Improved Antibacterial Activity Using Silica Shells Modified with Quaternary Ammonium Polyethyleneimine as a Bacterial Cell-Targeting Agent. *J. Agric. Food Chem.* **2021**, *69*, 6485–6494. [[CrossRef](#)]
50. Mas, N.; Galiana, I.; Mondragón, L.; Aznar, E.; Climent, E.; Cabedo, N.; Sancenón, F.; Murguía, J.R.; Martínez, L.M.; Marcos, M.D.; et al. Enhanced Efficacy and Broadening of Antibacterial Action of Drugs via the Use of Capped Mesoporous Nanoparticles. *Chem. A Eur. J.* **2013**, *19*, 11167–11171. [[CrossRef](#)]
51. Nurchi, V.M.; Crisponi, G.; Crespo-Alonso, M.; Lachowicz, J.I.; Szewczuk, Z.; Cooper, G.J.S. Complex formation equilibria of CuII and ZnII with triethylenetetramine and its mono- and di-acetyl metabolites. *Dalton Trans.* **2013**, *42*, 6161–6170. [[CrossRef](#)]
52. Lachowicz, J.I.; Delpiano, G.R.; Zanda, D.; Piludu, M.; Sanjust, E.; Monduzzi, M.; Salis, A. Adsorption of Cu²⁺ and Zn²⁺ on SBA-15 mesoporous silica functionalized with triethylenetetramine chelating agent. *J. Environ. Chem. Eng.* **2019**, *7*, 103205. [[CrossRef](#)]
53. Kim, S.T.; Chompoosor, A.; Yeh, Y.-C.; Agasti, S.; Solfiell, D.J.; Rotello, V.M. Dendronized Gold Nanoparticles for siRNA Delivery. *Small* **2012**, *8*, 3253–3256. [[CrossRef](#)]
54. Gottenbos, B.; Grijpma, D.W.; Van Der Mei, H.C.; Feijen, J.; Busscher, H.J. Antimicrobial effects of positively charged surfaces on adhering Gram-positive and Gram-negative bacteria. *J. Antimicrob. Chemother.* **2001**, *48*, 7–13. [[CrossRef](#)] [[PubMed](#)]
55. Villegas, M.F.; Garcia-Uriostegui, L.; Rodríguez, O.; Izquierdo-Barba, I.; Salinas, A.J.; Toriz, G.; Vallet-Regí, M.; Delgado, E. Lysine-Grafted MCM-41 Silica as an Antibacterial Biomaterial. *Bioengineering* **2017**, *4*, 80. [[CrossRef](#)]
56. Lowe, B.M.; Skylaris, C.-K.; Green, N.G. Acid-base dissociation mechanisms and energetics at the silica–water interface: An activationless process. *J. Colloid Interface Sci.* **2015**, *451*, 231–244. [[CrossRef](#)] [[PubMed](#)]
57. Apella, M.C.; Baran, E.J. The Infrared Spectra of Some Sulfate-Apatites. *Spectrosc. Lett.* **1979**, *12*, 1–6. [[CrossRef](#)]
58. Dindar, M.H.; Yaftian, M.R.; Rostamnia, S. Potential of functionalized SBA-15 mesoporous materials for decontamination of water solutions from Cr(VI), As(V) and Hg(II) ions. *J. Environ. Chem. Eng.* **2015**, *3*, 986–995. [[CrossRef](#)]
59. Fukahori, S.; Fujiwara, T.; Ito, R.; Funamizu, N. pH-Dependent adsorption of sulfa drugs on high silica zeolite: Modeling and kinetic study. *Desalination* **2011**, *275*, 237–242. [[CrossRef](#)]
60. Medda, L.; Casula, M.F.; Monduzzi, M.; Salis, A. Adsorption of Lysozyme on Hyaluronic Acid Functionalized SBA-15 Mesoporous Silica: A Possible Bioadhesive Depot System. *Langmuir* **2014**, *30*, 12996–13004. [[CrossRef](#)]
61. Ho, Y.-S. Selection of optimum sorption isotherm. *Carbon* **2004**, *42*, 2115–2116. [[CrossRef](#)]
62. Jia, X.; Li, S.; Wang, Y.; Ang, T.W.; Hou, X. Adsorption Behavior and Mechanism of Sulfonamide Antibiotics in Aqueous Solution on a Novel MIL-101(Cr)@GO Composite. *J. Chem. Eng. Data* **2019**, *64*, 1265–1274. [[CrossRef](#)]
63. Boreen, A.L.; Arnold, W.; McNeill, K. Photochemical Fate of Sulfa Drugs in the Aquatic Environment: Sulfa Drugs Containing Five-Membered Heterocyclic Groups. *Environ. Sci. Technol.* **2004**, *38*, 3933–3940. [[CrossRef](#)]
64. Nairi, V.; Medda, L.; Monduzzi, M.; Salis, A. Adsorption and release of ampicillin antibiotic from ordered mesoporous silica. *J. Colloid Interface Sci.* **2017**, *497*, 217–225. [[CrossRef](#)] [[PubMed](#)]
65. Lee, C.-H.; Lo, L.-W.; Mou, C.-Y.; Yang, C.-S. Synthesis and Characterization of Positive-Charge Functionalized Mesoporous Silica Nanoparticles for Oral Drug Delivery of an Anti-Inflammatory Drug. *Adv. Funct. Mater.* **2008**, *18*, 3283–3292. [[CrossRef](#)]
66. Climent, E.; Martínez-Mañez, R.; Sancenón, F.; Marcos, M.D.; Soto, J.; Maquieira, A.; Amorós, P. Controlled Delivery Using Oligonucleotide-Capped Mesoporous Silica Nanoparticles. *Angew. Chem. Int. Ed.* **2010**, *49*, 7281–7283. [[CrossRef](#)]
67. FDA. Trimethoprim with sulfamethoxazole (Bactrim) in gastroenterology [TRIMETHOPRIM SULFAMETHOXAZOL (BACTRIM) IN DER GASTROENTEROLOGIE]. *Praxis* **1974**, *63*, 680–684.
68. Yoshikawa, T.T.; Guze, L.B. Concentrations of Trimethoprim-Sulfamethoxazole in Blood After a Single, Large Oral Dose. *Antimicrob. Agents Chemother.* **1976**, *10*, 462–463. [[CrossRef](#)]
69. Schwartz, D.E.; Rieder, J. Pharmacokinetics of Sulfamethoxazole plus Trimethoprim in Man and Their Distribution in the Rat. *Chemotherapy* **1970**, *15*, 337–355. [[CrossRef](#)]
70. Dao, B.D.; Barreto, J.N.; Wolf, R.C.; Dierkhising, R.A.; Plevak, M.F.; Tosh, P.K. Serum peak sulfamethoxazole concentrations demonstrate difficulty in achieving a target range: A retrospective cohort study. *Curr. Ther. Res.* **2014**, *76*, 104–109. [[CrossRef](#)]
71. Lachowicz, J.I.; Emwas, A.; Delpiano, G.R.; Salis, A.; Piludu, M.; Jaremko, L.; Jaremko, M. Improving Metal Adsorption on Triethylenetetramine (TETA) Functionalized SBA-15 Mesoporous Silica Using Potentiometry, EPR and ssNMR. *Adv. Mater. Interfaces* **2020**, *7*. [[CrossRef](#)]
72. Brunauer, S.; Emmett, P.H.; Teller, E. Adsorption of Gases in Multimolecular Layers. *J. Am. Chem. Soc.* **1938**, *60*, 309–319. [[CrossRef](#)]
73. Barrett, E.P.; Joyner, L.G.; Halenda, P.P. The Determination of Pore Volume and Area Distributions in Porous Substances. I. Computations from Nitrogen Isotherms. *J. Am. Chem. Soc.* **1951**, *73*, 373–380. [[CrossRef](#)]
74. Da'Na, E.; De Silva, N.; Sayari, A. Adsorption of copper on amine-functionalized SBA-15 prepared by co-condensation: Kinetics properties. *Chem. Eng. J.* **2011**, *166*, 454–459. [[CrossRef](#)]
75. Azizian, S. Kinetic models of sorption: A theoretical analysis. *J. Colloid Interface Sci.* **2004**, *276*, 47–52. [[CrossRef](#)] [[PubMed](#)]

76. Zhu, J.; Zhu, X.; Gu, J.; Zhao, L.; Jiang, L.; Qiu, Y. Effective adsorption and concentration of carnosine by nickel species within mesoporous silica. *LWT* **2016**, *74*, 211–218. [[CrossRef](#)]
77. Ayawei, N.; Ebelegi, A.N.; Wankasi, D. Modelling and Interpretation of Adsorption Isotherms. *J. Chem.* **2017**, *2017*, 1–11. [[CrossRef](#)]
78. Dil, E.A.; Ghaedi, M.; Asfaram, A.; Hajati, S.; Mehrabi, F.; Goudarzi, A. Preparation of nanomaterials for the ultrasound-enhanced removal of Pb²⁺ ions and malachite green dye: Chemometric optimization and modeling. *Ultrason. Sonochemistry* **2017**, *34*, 677–691. [[CrossRef](#)] [[PubMed](#)]
79. Steri, D.; Monduzzi, M.; Salis, A. Ionic strength affects lysozyme adsorption and release from SBA-15 mesoporous silica. *Microporous Mesoporous Mater.* **2013**, *170*, 164–172. [[CrossRef](#)]
80. Nieto, A.; Colilla, M.; Balas, F.; Vallet-Regí, M. Surface Electrochemistry of Mesoporous Silicas as a Key Factor in the Design of Tailored Delivery Devices. *Langmuir* **2010**, *26*, 5038–5049. [[CrossRef](#)]